

# Title: Quantum-inspired super-resolution of fluorescent point-like sources

Authors: Cheyenne S. Mitchell<sup>1,2</sup>, Dhananjay Dhruva<sup>2,3,4</sup>, Zachary P. Burke<sup>1</sup>, David J. Durden<sup>1,2</sup>, Armine I. Dingilian<sup>2,3,4</sup>, Mikael P. Backlund<sup>1,2,3,4\*</sup>

## Affiliations:

<sup>1</sup>Department of Chemistry, University of Illinois at Urbana-Champaign; Urbana, IL 61801, USA.

<sup>2</sup>Illinois Quantum Information Science and Technology Center (IQUIST), University of Illinois at Urbana-Champaign; Urbana, IL 61801, USA.

<sup>3</sup>Center for Biophysics and Quantitative Biology, University of Illinois at Urbana-Champaign; Urbana, IL 61801, USA.

<sup>4</sup>NSF Science and Technology Center for Quantitative Cell Biology, University of Illinois at Urbana-Champaign; Urbana, IL 61801, USA.

\*Corresponding author. Email: mikaelb@illinois.edu

**Abstract:** We report the experimental super-resolution of pairs of simultaneously emitting point-like fluorescent sources using a modified image inversion interferometer microscope. The technique is inspired by recent developments in the application of quantum parameter estimation theory to semiclassical imaging problems. We find that the image inversion technique requires special polarization filtering to account for the dipolar nature of the emission. Using an azimuthal polarizer, we obtain improvements in the Fisher information of point-source separation by over an order of magnitude relative to direct imaging. Unlike established super-resolution fluorescence techniques, the method does not require sequential photoswitching/blinking of the fluorophores, and thus could facilitate significant speed-ups for certain biological imaging/tracking tasks.

## Main Text:

In the context of optical imaging, resolving objects separated by distances less than the wavelength of light is fundamentally difficult (Fig. 1A). This basic fact of physics has been appreciated since it was articulated in the works of Abbe (1) and Rayleigh (2) during the latter half of the nineteenth century. According to Rayleigh's criterion, when the separation of two point sources is less than  $\sim 0.61 \lambda/\text{NA}$  (where  $\lambda$  is the wavelength of light and NA is the imaging system's numerical aperture) they are rendered unresolvable. The development of classical statistical inference in the century-plus since Rayleigh calls for some refinement of this statement, as given enough measurement averaging (i.e. a sufficient number of detected photons) one can always discern between the binary hypotheses of one vs. two emitters with an arbitrarily small error rate. One popular reformulation of Rayleigh's criterion invokes the Fisher information (FI) (3), a figure-of-merit that governs one's ability to extract a precise estimate of one or more parameters from a set of noisy observations (4). "Rayleigh's curse" says that the FI with respect to estimating the separation distance between two emitters vanishes as the separation goes to zero (5, 6). Equivalently, the inverse of the FI, the Cramér-Rao bound (CRB), diverges in the same limit.

In the broader context of quantum parameter estimation theory, the classical FI is bounded above by the more fundamental quantum Fisher information (QFI) (7). From this vantage, Tsang, Nair, and Lu recently proved that Rayleigh’s curse is illusory in some sense (5). Whereas the FI associated with “direct imaging” (i.e. a pixel-resolved intensity measurement at a conjugate image plane) vanishes in the limit of zero separation, the QFI in fact remains constant. This means that some measurement scheme other than direct imaging can in principle resolve two point objects deep in the subdiffraction regime much more efficiently than can be done via direct imaging. Said differently, direct imaging effectively leaves information contained in the phase of the light unharvested. An appropriately chosen phase-sensitive measurement can recover this lost information. To be clear, despite the fact that the calculation of QFI begins with the density operator describing the quantum electromagnetic field, overcoming Rayleigh’s curse does not depend on multi-particle entanglement. It only requires phase coherence in the light. Indeed, the result can be retrofitted into the language of semiclassical detection theory where the hidden information is contained in the phase of the classical electromagnetic field (8). Tsang and coworkers’ seminal paper has since spawned a flurry of follow-up theoretical and experimental work as reviewed in Ref. (6); the emerging area is collectively referred to as “quantum-inspired super-resolution”.

From the outset, Tsang, Nair, and Lu proposed a measurement based on spatial-mode demultiplexing (SPADE) to saturate the QFI (5, 6, 8–14). For a Gaussian point-spread function (PSF), this corresponds to photon counting in the basis of Hermite-Gaussian transverse modes (5). For a more general PSF (e.g., an Airy disk), the optimal basis for SPADE can be constructed algorithmically (15). A related proposal based on image inversion interferometry (which we will refer to as “III” but has also been called SLIVER) effectively sorts into even- and odd-parity transverse spatial modes, which is in theory sufficient to break Rayleigh’s curse for two closely spaced point emitters (13, 16, 17). The idea is that a single point source located on the optical axis will produce an even-parity field, and as such all the collected light will be shunted to one of the two interferometer outputs. Now if the position deviates slightly from the optical axis, a few photons will be recorded in the odd-parity channel, such that by sitting on this dark fringe the measurement can be made very sensitive to displacement of the source from the optical axis. The last ingredient in translating this into source pair super-resolution is to align the system such that the optical axis coincides with the average position of the pair (which is considerably easier to estimate from direct imaging than is separation). While SPADE and its variants promise a new route to super-resolution imaging in microscopy, telemetry, and everything between, the experimental demonstrations published to date have tended to target a pair of laser spots with spoiled mutual coherence (11, 12, 16, 18–20). In this work we report the experimental demonstration of quantum-inspired super-resolution in the context of fluorescence microscopy.

Of course, a suite of Nobel-prize-winning super-resolution fluorescence microscopy techniques already exist in the forms of PALM/STORM (21–23), STED (24, 25), and variations thereof (26, 27). Before proceeding we must place quantum-inspired super-resolution against this backdrop. Both the PALM/STORM and STED routes to super-resolution depend on the controlled photoswitching of fluorophores. For PALM/STORM in particular this means stochastically separating the emission events of neighboring molecules in time, and as a result these methods are often prohibitively slow. MINIFLUX microscopy has recently been used to achieve unprecedented resolutions (28–31), but still typically relies on stochastic switching of the labels. By contrast, quantum-inspired schemes do not require photoswitching, and so can in principle be used to super-resolve much more dynamic scenes labeled using a broader class of fluorescent emitters.

## Concept and Theory

Figure 1B in part restates Tsang, Nair, and Lu’s main theoretical result (5), but with one important revision. The original theory invoked the scalar approximation to effectively treat a pair of monopole emitters. In nature, however, there are no monopole emitters of electromagnetic radiation. A real “isotropic” point source consists of an ensemble of randomly oriented dipole emitters, the emission of which can be modeled as a mixture of  $x$ -,  $y$ -, and  $z$ -oriented dipole emitters (32). The data depicted in Fig. 1B result from a full vectorial diffraction calculation, wherein both isotropic point sources are modeled as a mixture of dipole emitters. For direct imaging, the result is qualitatively the same. The FI for direct imaging (blue line) vanishes at small separation despite the constant QFI. At a separation of 5 nm, the QFI is more than 3 orders of magnitude larger than the FI of direct imaging, meaning that there exists some measurement scheme other than direct imaging that can achieve a given resolution benchmark with fewer than  $10^{-3}$  times as many detected photons. For our experimental pursuit of quantum-inspired super-resolution, we elected to construct a microscope based on image inversion interferometry (III, Fig. 2). However, a calculation of the FI of separation based on III as previously proposed yielded some initially sobering results (red line). Whereas the proposed III would yield significant enhancement in the resolution of monopole emitters, it evidently only leads to a modest improvement over direct imaging when targeting more realistic isotropic emitters. To wit, at 5 nm separation the FI associated with III is only about a factor of 3 larger than that of direct imaging. The loss of performance can be understood in terms of the symmetry of the fields emitted by dipoles of different orientations. Taking  $z$  to be parallel to the optical axis, emission from a dipole oriented perpendicular to  $z$  produces emission that is symmetric with respect to inversion about the centroid (Fig. S1). Thus a dipole oriented perpendicular to  $z$  and positioned on the optical axis will produce a null in one output port of the III, just the same as it would for a monopole emitter. On the other hand, a dipole oriented parallel to  $z$  emits a field that is anti-symmetric with respect to inversion about the centroid. A dipole parallel to  $z$  and positioned on the optical axis will produce a null in the *other output port* of the III (Fig. S1). If you know your dipole emitters are oriented either perpendicular or parallel to  $z$ , then the III would in principle work as advertised. However, if the collected light comes from the emission of a dipole with some intermediate orientation or a mixture of dipoles with different-symmetry emission, then neither output port can be nulled perfectly (Fig. S1). The resulting inability to “sit on a dark fringe” is precisely why the original design of the III fails to produce much improvement over direct imaging for a real isotropic emitter. We comment here that this effect should only be important for high-NA imaging systems. When the NA is very low, the fraction of light collected from dipoles bearing a significant component parallel to  $z$  is small, and so in this limit the collected field is effectively inversion symmetric. However, state-of-the-art fluorescence microscopes almost always employ high-NA objectives, meaning the effect of incomplete nulling cannot be ignored in this case. The calculations depicted in Fig. 1B model the NA = 1.45 oil objective we use in our experiments.

Thankfully, we soon recognized a way to salvage the super-resolving power of the III microscope by appropriate filtering of the polarization. At the Fourier plane of the microscope, if one resolves the light collected due to dipolar emission into the azimuthal and radial polarization basis, it is known that the azimuthally polarized portion is guaranteed to be anti-symmetric with respect to inversion, and that all of the asymmetry, if there is any, will be carried entirely by the radially polarized light (33, 34). Thus, by throwing away the radially polarized light, one can

recover the ability to sit on a dark fringe. Filtering the radially polarized light emitted by an isotropic source in this way and then injecting into the III results in an FI for source separation that is vastly improved relative to direct imaging or unpolarized III (Fig. 1B, gold line). Only a modest factor of about 1.6 separates the FI of this polarized III scheme from the QFI. The small persisting gap can be closed by mining the scraps of information contained in the radial channel, but for an isotropic point source this is almost certainly more trouble than it's worth.

## Results and Discussion

To experimentally realize this polarization-filtered version of III we constructed the setup depicted in Fig. 2. Two Dove prisms oriented orthogonal to one another and placed in opposite arms of the interferometer effect the image inversion. To achieve the desired polarization filtering, we added a vortex half wave plate to the III at a particular plane in the collection path. The vortex plate converts azimuthally polarized light into  $y$  and radial into  $x$  (34). The asymmetric part of the light can then be rejected by inserting a linear polarizer. The vortex phase shift renders the image of a single point source as a donut, akin to the excitation PSF in MINIFLUX (28–31) and the stimulated emission beam in STED (24, 25).

The experimental procedure we employed essentially constitutes an analog simulation of a pair of mutually incoherent point-like isotropic emitters separated by a range of subdiffraction distances (see Fig. S2 and Materials and Methods section). We recorded tens-of-thousands of images of isolated 40-nm fluorescent beads as their position was scanned in the proximity of the optical axis with a piezo stage. Images of the same bead recorded at opposing positions were combined in post-processing to emulate the source pair. A “ground truth” of separation was established by first recording calibration images in which the image of a target bead is well separated from its inverted dual. The target bead and a separate fiducial bead could then both be individually super-localized by fitting to a simplified PSF model. Then the target was scanned near the optical axis such that the inverted image pair overlapped and interfered with one another. In these images, the still-isolated fiducial was super-localized, and from this localization we triangulated the ground-truth position of the target relative to the optical axis.

The recorded images were then combined and analyzed using a custom MATLAB routine, the output of which is a library of filtered images of source pairs on a grid of subdiffraction separations. A subset of this library is depicted in Fig. 3A-E for a sampling of subdiffraction separations,  $\Delta x$ , oriented parallel to the horizontal axis of the image. (Additional slices of the library can be found in Fig. S3.) In Channel 1, constructive interference yields a single bright donut that does not change much as a function of small separations. The lion's share of the information is conveyed in Channel 2, where destructive interference leads to near-perfect nulling when the separation approaches zero. As the separation increases, a bowtie shape appears and becomes increasingly bright.

For fair comparison we repeated our experimental procedure with two important modifications. First, the vortex half wave plate and linear polarizer were removed such that the image of a point source again resembled a singly peaked Gaussian. Second, one of the delay stages within the interferometer was displaced such that the coherence between the two arms was destroyed. In this way we could emulate direct imaging in a manner that lends itself to analysis with the same software. For reference, the results of this control are shown in Fig. 3F-J. One can immediately

appreciate that direct imaging will struggle in resolving source pairs by observing how little the images change across the panels.

To lend some quantitation to the assessment of our III microscope we computed the fringe visibility as defined by:

$$V(\Delta x, \Delta y) = \frac{I_1(\Delta x, \Delta y) - I_2(\Delta x, \Delta y)}{I_1(\Delta x, \Delta y) + I_2(\Delta x, \Delta y)}$$

where  $I_1$  and  $I_2$  indicate the background-corrected total intensity in Channels 1 and 2, respectively. Results are plotted in Fig. 3K. For comparison, the visibilities obtained from our direct imaging control are displayed in Fig. 3L.

Digging deeper into the data, our image libraries allow us to compute the realized FI with respect to separation for each imaging modality. In every case we found that the FIs computed in this way were lower than those predicted from calculations, presumably due to experimental non-idealities that are not captured by the theoretical model, such as residual phase aberrations and pupil apodization. A comparison among the imaging modalities is nonetheless meaningful. Fig. 4A sketches the experimentally recovered FIs for polarized III imaging (gold) as well as for the direct imaging control (blue). Importantly, we note that the FI for polarized III in this display has already been diminished by a factor of 0.647 to assess a penalty for throwing away the radially polarized light. At a separation of 5 nm, the FI associated with polarized III is roughly 35x larger than that of the direct imaging control. We evidently do not realize the full 3 orders of magnitude improvement predicted by theory, but we nonetheless improve by more than one order of magnitude.

As an additional control, we sought to parse the observed improvement into contributions from the change in PSF shape vs. that due to the interferometry. Indeed, our theory-based calculation predicts that direct imaging with the donut PSF should improve the FI at a separation of 5 nm by about a factor of 16 relative to ordinary direct imaging. To perform the experiment, we left the vortex half wave plate and linear polarizer in place, but displaced one of the delay lines in the interferometer to spoil the coherence. The experimentally recovered FI for this “direct donut” imaging modality (Fig. 4A, green) is about twice that of ordinary direct imaging at 5 nm separation. We conclude that some of the resolution enhancement realized in comparing the polarized III to ordinary direct imaging is due to the change in shape of the PSF, but most of the effect can be attributed to the interferometer.

We evaluated experimental performance of each of these three imaging modalities in yet another way by generating separation estimates from carefully paired noisy images, then computing the mean-squared error (MSE) of this estimate relative to the “ground truth” obtained from triangulating the position of the fiducial. For ordinary direct imaging we estimated separation based on a least-squares fit to a pair of Gaussian spots. For donut direct imaging we estimated separation similarly, but using a donut-shaped PSF model. For the polarized III data, we compared the processed image library from one day’s worth of data to the noisy images recorded on a different day, then produced an estimate of separation by finding the minimum mean-squared error between the model and the noisy image. (Results from additional data and alternative estimators are given in Fig. S4.) At the particular signal-to-noise ratio we worked at (which was throttled by the need to collect many images over an extended period of time), we



found that the separation estimator used for both kinds of direct imaging exhibit significant biases. Since CRB (the inverse of the FI) is guaranteed only to lower-bound the variance of any *unbiased* estimator, we might not necessarily expect the MSEs depicted in Fig. 4B to look like the inverses of the curves in Fig. 4A. Nonetheless, at 5 nm separation we find that ordinary direct imaging produced a mean MSE over an order of magnitude worse than that derived from polarized III.

## Conclusions

We have revised the theory of image inversion interferometry to account for the direction- and polarization-dependent emission of real point sources. With appropriate polarization filtering, the III can indeed beat Rayleigh's curse. We constructed an III microscope and carefully benchmarked its experimental performance, effectively demonstrating quantum-inspired super-resolution imaging. While the experimentally realized resolution enhancement is significant, theory predicts a great deal of room to improve. One upgrade to the setup to be implemented in the future is to correct phase aberrations individually in both arms of the interferometer, as suggested in (35). We also suspect that apodization due to imperfections in one or more optical components may have limited our performance. The finite size of the fluorescent beads used (40 nm) likely diminished the apparent resolution of each imaging modality as well. Smaller beads or quantum emitters could be used, but at the cost of reduced brightness and/or photostability.

Our microscope enables a new route to super-resolution in fluorescence microscopy that does not depend on photoswitching of the emitters. This expands the list of compatible fluorescent labels and could lead to significant speed-ups in certain biological imaging/tracking applications. Of course, our experiments only demonstrate super-resolution on a very simple scene consisting of two point sources. It's unclear how its performance might translate to more complicated scenes (36–40). Thus, in cases where very little prior information is available about the scene, established super-resolution fluorescence techniques will likely still reign supreme. On the other hand, in cases where one knows their scene consists of just two sources (e.g., in tracking gene loci in diploid cells (41)), the method could prove powerful. We also expect to find utility in efficiently estimating the size and shape of subdiffraction objects (8, 9).

- 
1. E. Abbe, Beiträge zur Theorie des Mikroskops und der mikroskopischen Wahrnehmung. *Arch. Für Mikrosk. Anat.* **9**, 413–468 (1873).
  2. Rayleigh, XXXI. *Investigations in optics, with special reference to the spectroscope.* *Lond. Edinb. Dublin Philos. Mag. J. Sci.* **8**, 261–274 (1879).
  3. J. Chao, E. S. Ward, R. J. Ober, Fisher information theory for parameter estimation in single molecule microscopy: tutorial. *JOSA A* **33**, B36–B57 (2016).
  4. H. L. Van Trees, *Detection, Estimation, and Modulation Theory, Part I: Detection, Estimation, and Linear Modulation Theory* (John Wiley & Sons, 2004).
  5. M. Tsang, R. Nair, X.-M. Lu, Quantum Theory of Superresolution for Two Incoherent Optical Point Sources. *Phys. Rev. X* **6**, 031033 (2016).
  6. M. Tsang, Resolving starlight: a quantum perspective. *Contemp. Phys.* (2019).
  7. Quantum detection and estimation theory | Journal of Statistical Physics.  
<https://link.springer.com/article/10.1007/bf01007479>.

8. M. Tsang, Subdiffraction incoherent optical imaging via spatial-mode demultiplexing: Semiclassical treatment. *Phys. Rev. A* **97**, 023830 (2018).
9. M. Tsang, Subdiffraction incoherent optical imaging via spatial-mode demultiplexing. *New J. Phys.* **19**, 023054 (2017).
10. X.-J. Tan, L. Qi, L. Chen, A. J. Danner, P. Kanchanawong, M. Tsang, Quantum-inspired superresolution for incoherent imaging. *Optica* **10**, 1189–1194 (2023).
11. P. Boucher, C. Fabre, G. Labroille, N. Treps, Spatial optical mode demultiplexing as a practical tool for optimal transverse distance estimation. *Optica* **7**, 1621–1626 (2020).
12. C. Rouvière, D. Barral, A. Grateau, I. Karuseichyk, G. Sorelli, M. Walschaers, N. Treps, Ultra-sensitive separation estimation of optical sources. *Optica* **11**, 166–170 (2024).
13. R. Nair, M. Tsang, Far-Field Superresolution of Thermal Electromagnetic Sources at the Quantum Limit. *Phys. Rev. Lett.* **117**, 190801 (2016).
14. S. Z. Ang, R. Nair, M. Tsang, Quantum limit for two-dimensional resolution of two incoherent optical point sources. *Phys. Rev. A* **95**, 063847 (2017).
15. J. Rehacek, M. Paúr, B. Stoklasa, Z. Hradil, L. L. Sánchez-Soto, Optimal measurements for resolution beyond the Rayleigh limit. *Opt. Lett.* **42**, 231–234 (2017).
16. Z. S. Tang, K. Durak, A. Ling, Fault-tolerant and finite-error localization for point emitters within the diffraction limit. *Opt. Express* **24**, 22004–22012 (2016).
17. R. Nair, M. Tsang, Interferometric superlocalization of two incoherent optical point sources. *Opt. Express* **24**, 3684–3701 (2016).
18. L. Santamaria, D. Pallotti, M. S. de Cumis, D. Dequal, C. Lupo, Spatial-mode-demultiplexing for enhanced intensity and distance measurement. *Opt. Express* **31**, 33930 (2023).
19. W.-K. Tham, H. Ferretti, A. M. Steinberg, Beating Rayleigh’s Curse by Imaging Using Phase Information. *Phys. Rev. Lett.* **118**, 070801 (2017).
20. W. Larson, N. V. Tabiryan, B. E. A. Saleh, A common-path polarization-based image-inversion interferometer. *Opt. Express* **27**, 5685–5695 (2019).
21. E. Betzig, G. H. Patterson, R. Sougrat, O. W. Lindwasser, S. Olenych, J. S. Bonifacino, M. W. Davidson, J. Lippincott-Schwartz, H. F. Hess, Imaging Intracellular Fluorescent Proteins at Nanometer Resolution. *Science* **313**, 1642–1645 (2006).
22. S. T. Hess, T. P. K. Girirajan, M. D. Mason, Ultra-High Resolution Imaging by Fluorescence Photoactivation Localization Microscopy. *Biophys. J.* **91**, 4258–4272 (2006).
23. M. J. Rust, M. Bates, X. Zhuang, Sub-diffraction-limit imaging by stochastic optical reconstruction microscopy (STORM) | Nature Methods. *Nat. Methods* **3**, 793–796 (2006).
24. S. W. Hell, J. Wichmann, Breaking the diffraction resolution limit by stimulated emission: stimulated-emission-depletion fluorescence microscopy. *Opt. Lett.* **19**, 780–782 (1994).
25. T. A. Klar, S. Jakobs, M. Dyba, A. Egner, S. W. Hell, Fluorescence microscopy with diffraction resolution barrier broken by stimulated emission. *Proc. Natl. Acad. Sci.* **97**, 8206–8210 (2000).
26. L. Schermelleh, A. Ferrand, T. Huser, C. Eggeling, M. Sauer, O. Biehlmaier, G. P. C. Drummen, Super-resolution microscopy demystified. *Nat. Cell Biol.* **21**, 72–84 (2019).
27. S. Liu, P. Hoess, J. Ries, Super-Resolution Microscopy for Structural Cell Biology. *Annu. Rev. Biophys.* **51**, 301–326 (2022).
28. F. Balzarotti, Y. Eilers, K. C. Gwosch, A. H. Gynna, V. Westphal, F. D. Stefani, J. Elf, S. W. Hell, Nanometer resolution imaging and tracking of fluorescent molecules with minimal photon fluxes | Science. *Science* **355**, 606–612 (2017AD).

29. R. Schmidt, T. Weihs, C. A. Wurm, I. Jansen, J. Rehman, S. J. Sahl, S. W. Hell, MINFLUX nanometer-scale 3D imaging and microsecond-range tracking on a common fluorescence microscope | Nature Communications. *Nat. Commun.* **12**, 1478 (2021).
30. K. C. Gwosch, J. K. Pape, F. Balzarotti, P. Hoess, J. Ellenberg, J. Ries, S. W. Hell, MINFLUX nanoscopy delivers 3D multicolor nanometer resolution in cells. *Nat. Methods* **17**, 217–224 (2020).
31. S. J. Sahl, J. Matthias, K. Inamdar, M. Weber, T. A. Khan, C. Brüser, S. Jakobs, S. Becker, C. Griesinger, J. Broichhagen, S. W. Hell, Direct optical measurement of intramolecular distances with angstrom precision. *Science*, doi: 10.1126/science.adj7368 (2024).
32. A. S. Backer, W. E. Moerner, Extending Single-Molecule Microscopy Using Optical Fourier Processing. *J. Phys. Chem. B* **118**, 8313–8329 (2014).
33. M. D. Lew, W. E. Moerner, Azimuthal Polarization Filtering for Accurate, Precise, and Robust Single-Molecule Localization Microscopy. *Nano Lett.* **14**, 6407–6413 (2014).
34. M. P. Backlund, A. Arbabi, P. N. Petrov, E. Arbabi, S. Saurabh, A. Faraon, W. E. Moerner, Removing orientation-induced localization biases in single-molecule microscopy using a broadband metasurface mask | Nature Photonics. *Nat. Photonics* **10**, 459–462 (2016).
35. D. J. Schodt, P. J. Cutler, F. E. Becerra, K. A. Lidke, Tolerance to aberration and misalignment in a two-point-resolving image inversion interferometer. *Opt. Express* **31**, 16393–16405 (2023).
36. M. R. Grace, Z. Dutton, A. Ashok, S. Guha, Approaching quantum-limited imaging resolution without prior knowledge of the object location. *J. Opt. Soc. Am. A* **37**, 1288 (2020).
37. S. Zhou, L. Jiang, Modern description of Rayleigh’s criterion. *Phys. Rev. A* **99**, 013808 (2019).
38. J. Řeháček, Z. Hradil, B. Stoklasa, M. Paúr, J. Grover, A. Krzic, L. L. Sánchez-Soto, Multiparameter quantum metrology of incoherent point sources: Towards realistic superresolution. *Phys. Rev. A* **96**, 062107 (2017).
39. J. Řeháček, Z. Hradil, D. Koutný, J. Grover, A. Krzic, L. L. Sánchez-Soto, Optimal measurements for quantum spatial superresolution. *Phys. Rev. A* **98**, 012103 (2018).
40. C. Lupo, Z. Huang, P. Kok, Quantum Limits to Incoherent Imaging are Achieved by Linear Interferometry. *Phys. Rev. Lett.* **124**, 080503 (2020).
41. M. Backlund, R. Joyner, K. Weis, W. E. Moerner, Correlations of three-dimensional motion of chromosomal loci in yeast revealed by the double-helix point spread function microscope. **25**, 3619–3629 (2014).

**Acknowledgements:** We thank Dongbeom Kim, Gina Lorenz, Paul Kwiat, Simeon Bogdanov, Ali Passian, Sam Bhagia, and Patrick Snyder for fruitful discussions.

**Funding:** This research was supported by the Department of Energy grant DE-SC0023167 (to CSM and MPB). Additional support due to the National Science Foundation grant 2243257 (to DD, AID, and MPB).

**Author contributions:** CSM, DD, and ZPB constructed the apparatus and performed the experiments. MPB, CSM, and DD analyzed the data. MPB performed the theory and computations. DJD provided support in interfacing software and hardware. AID provided theory support. MPB conceived of the project.

The authors declare no competing interests.



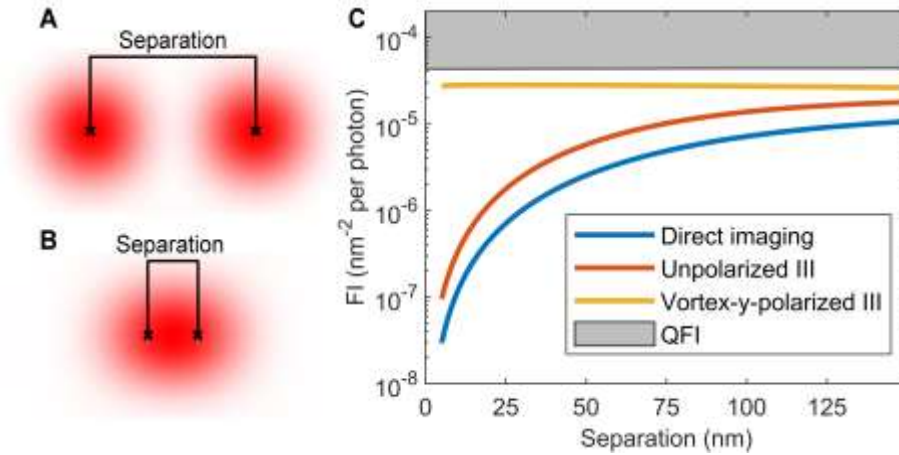


**Fig. 1: Illustration of point source separation and theoretical Fisher information calculations.** Calculated direct images of a pair of isotropic point emitters at (A) easily resolved and (B) subdiffraction separations. (C) Fisher information with respect to separation of a pair of realistic isotropic emitters, derived from vectorial diffraction calculations. The gray box is bounded below by the quantum limit. Our polarized image inversion scheme nearly saturates the quantum bound (gold), while both unpolarized image inversion and direct imaging fair much worse.

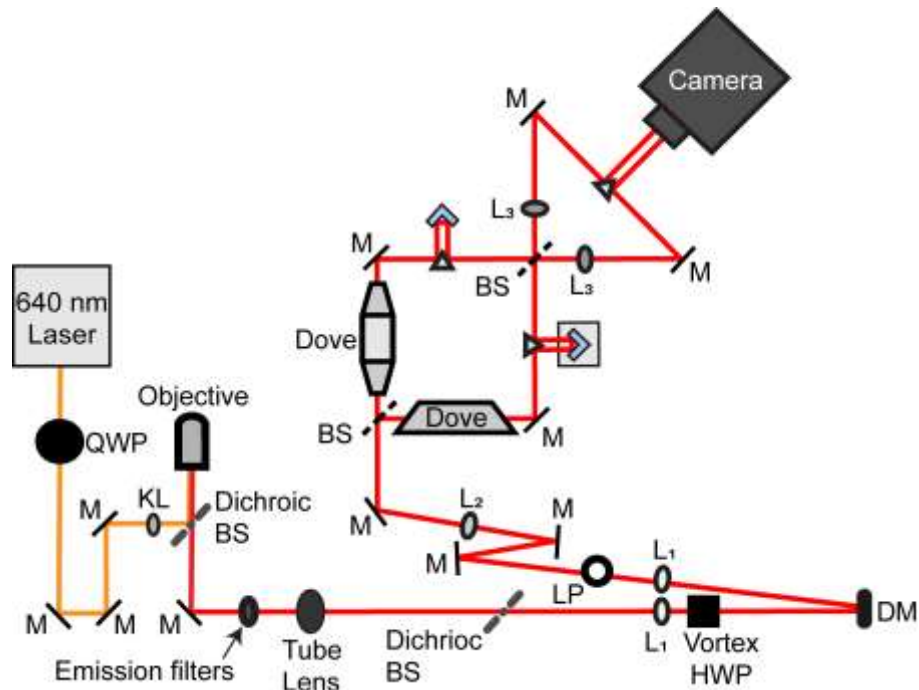


**Fig. 2: Experimental Setup**

Schematic of setup used to realize quantum-inspired super-resolution via polarized image inversion interferometry. QWP: quarter wave plate, M: mirror, KL: Köhler lens, BS: beam splitter, L: lens, Vortex HWP: vortex half wave plate, DM: deformable mirror, LP: linear polarizer. The second dichroic BS placed just after the tube lens compensates for birefringence due to the first dichroic BS. The deformable mirror is used to correct for phase aberrations. The vortex HWP and LP combine to reject the radially polarized emission.

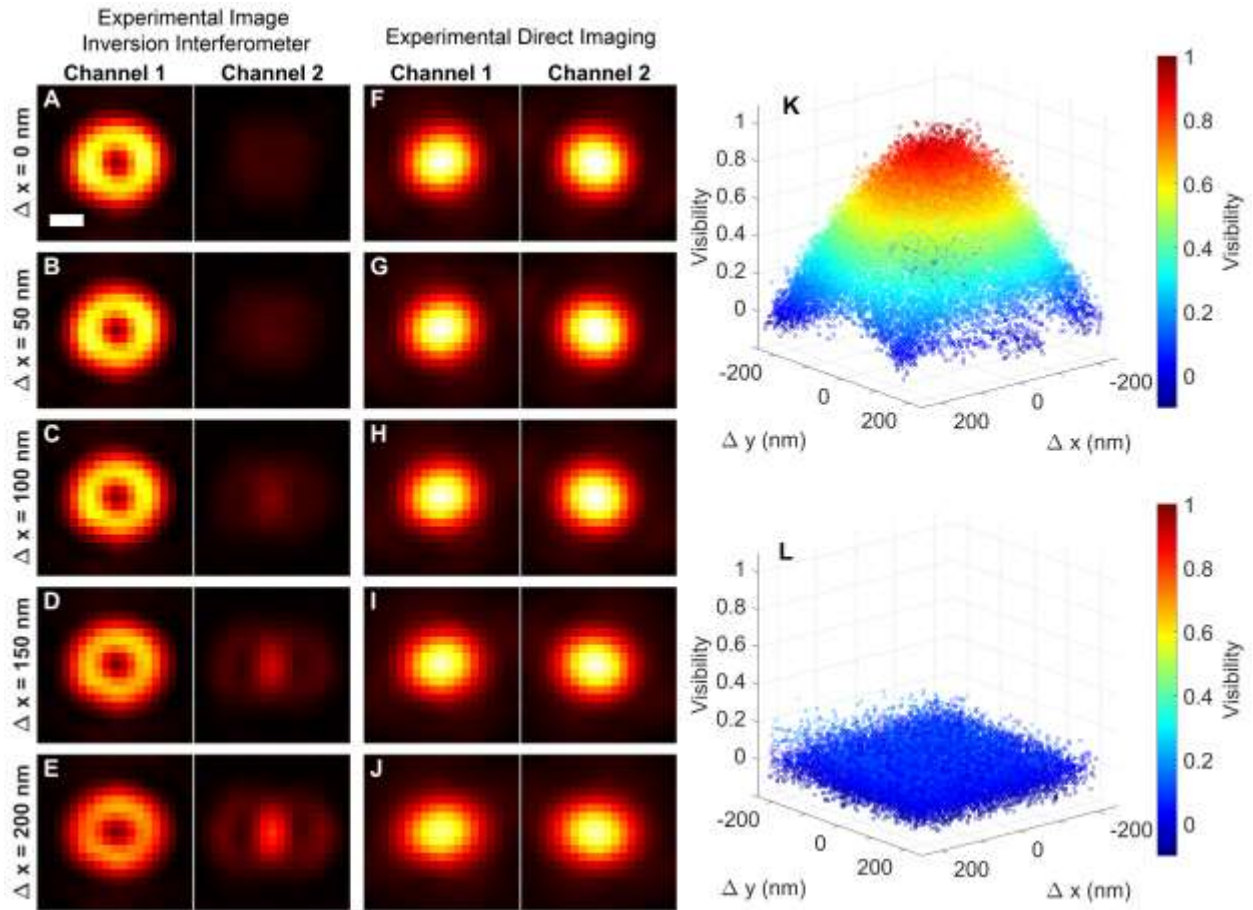


**Fig. 3: Experimentally derived images and associated fringe visibilities.** (A-E) Depicts the processed images resulting in both of the two channels of the polarized image inversion microscope for various point source separations. (F-J) Shows that corresponding processed images for a control experiment in which the polarizing elements were removed and the coherence between the arms of the interferometer was spoiled, effectively producing two direct imaging experiments. (K) Experimental fringe visibility realized by the polarized image inversion microscope. (L) Fringe visibility of the control. Scale bar: 250 nm.

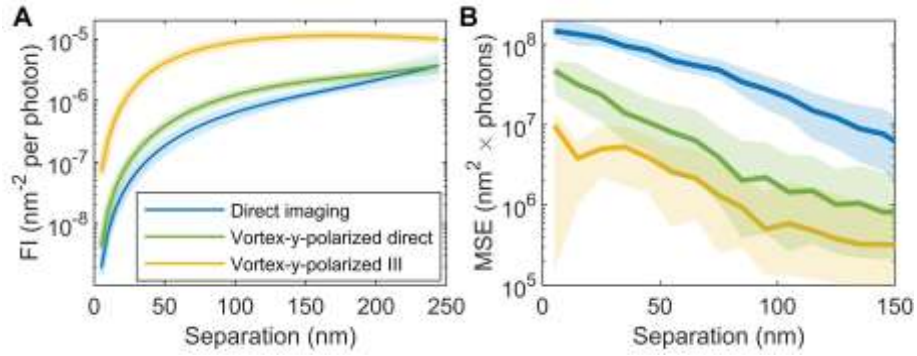


**Fig. 4: Experimental results.** (A) The Fisher information derived from processed experimental images of the polarized image inversion interferometer (gold) and direct imaging control (blue). Another control in which the polarizing elements were left in place to produce a donut PSF, but the coherence between the arms of the interferometer was spoiled is also included (green). Transparent lines: FI computed for separation vectors oriented along each of 10 directions between  $0^\circ$  and  $180^\circ$ . Solid lines: mean of FIs computed for different directions. (B) Apparent photon-scaled mean-squared error for each estimator of separation compared to the ground truth provided by triangulation from the position of a fiducial bead. Shaded regions are bounded by the 25<sup>th</sup> and 75<sup>th</sup> percentiles, while solid lines demarcate the median. Colors are the same as in (A).